Networks and Heterogeneous Media

http://www.aimspress.com/journal/nhm

NHM, 20(2): 648–669.
DOI: 10.3934/nhm.2025028
Received: 17 January 2025
Revised: 19 May 2025
Accepted: 28 May 2025
Published: 10 June 2025

Research article

Dynamic properties and numerical simulations of a fractional phytoplankton-zooplankton ecological model

Shuai Zhang[1], **Haolu Zhang**[2], **Yulan Wang**[1,*] **and Zhiyuan Li**[3]

[1] Department of Mathematics, Inner Mongolia University of Technology, Hohhot 010051, China

[2] School of Civil Engineering, Inner Mongolia University of Technology, Hohhot 010051, China

[3] College of Date Science and Application, Inner Mongolia University of Technology, Hohhot 010080, China

* **Correspondence:** Email: wylnei@imut.edu.cn.

Abstract: It is always a difficult and hot topic to effectively explore the dynamic behavior of phytoplankton-zooplankton models. Thus, we investigated dynamic properties and a numerical solution of a fractional-order phytoplankton-zooplankton ecological model (PZEM) that incorporates the effects of toxic substances and additional food transmission in the environment. First, stability, Turing instability, Hopf bifurcation, and weakly nonlinear analysis were analyzed for the PZEM. Second, a new high-precision numerical method was developed for the fractional PZEM without diffusion terms. We compared the method with other methods to determine the effectiveness of the present method. A discretization method was established for the PZEM with diffusion term. Finally, numerical simulation verified the feasibility of the theory. Numerical simulations showed the chaotic attractor and some novel pattern dynamical behaviors of the PZEM.

Keywords: chaotic attractor; pattern; numerical simulations; Hopf bifurcation analysis; phytoplankton-zooplankton model; weakly nonlinear analysis

1. Introduction

Due to the difficulty in measuring the biomass of plankton, mathematical models of plankton populations are important methods for understanding the physical and biological processes of plankton. Various phytoplankton-zooplankton models (PZMs) have been studied: An NPZD model [1], a stochastic PZM [2], a plankton-nutrient system [3], a marine phytoplankton-zooplankton ecological model (PZEM) [4], Trophic phytoplankton-zooplankton models (PZM) [5], a bioeconomic PZM with time delays [6], a two-zooplankton one-phytoplankton PZM [7], a phytoplankton and two

zooplankton PZM with toxin-producing delay [8], planktonic animal and plant PZM [9], and other PZMs [10–12]. In [12], Wang et al. investigated the following PZEM:

$$\begin{cases} \frac{dP}{dt} = \overbrace{rP\left(1-\frac{P}{K}\right)}^{plant\ growth} - \overbrace{\frac{e_1PZ}{1+e_1h_1P+e_2h_2A}}^{plant\ loss}, \\ \frac{dZ}{dt} = \underbrace{\frac{n_1e_1PZ+n_2e_2AZ}{1+e_1h_1P+e_2h_2A}}_{animal\ gain} - \underbrace{\tau Z}_{natural\ death} - \underbrace{\sigma\frac{PZ}{h+P}}_{animal\ death}. \end{cases} \tag{1.1}$$

Fractional-order reaction-diffusion equation can describe the dynamic behavior of real systems more accurately. In recent years, fractional-order models have made remarkable progress in fields such as biomedicine, ecology, and public health. In biomedicine, fractional-order models have been used to study tumor growth [13] and hepatitis B virus (HBV) treatment [14], revealing their advantages in describing the complex dynamic behaviors of biological systems. In ecology, fractional-order models have demonstrated their potential in the study of ecosystem complexity by analyzing the dynamic behaviors of plant-herbivore interactions [15]. In public health, the fractional model has been applied to analyze the transmission of smoking behavior [16] and the correlation between human papilloma virus (HPV) and cervical cancer [17], highlighting their utility in public health research. These studies not only enrich the theoretical application of fractional models but also have made significant progress in numerical analysis, providing new tools and methods for solving complex biomedical and ecological problems [13, 17]. For example, in ecology, fractional PZEMs can more accurately describe the complex dynamics of ecosystems, including population fluctuations and interactions. Li et al. [18] studied an established fractional-order delayed zooplankton-phytoplankton model. Javidi and Ahmad [19] studied dynamic analysis of time fractional-order phytoplankton-toxic PZM. Kumar et al. [20] studied a fractional plankton-oxygen modeling. The proposed fractional-order PZEM extends traditional integer-order models by incorporating memory effects through fractional derivatives, which better capture long-term ecological interactions. This model accounts for toxic substances and additional food transmission, factors critical to understanding algal blooms, and population collapse. Models often neglect cross-diffusion and fractional dynamics, limiting their ability to simulate complex spatiotemporal patterns. Our work bridges this gap, offering insights into chaotic attractors and pattern formation under realistic ecological constraints. In this paper, we investigate the following fractional-order PZEM:

$$\begin{cases} \frac{\partial^{\alpha_1}P}{\partial t^{\alpha_1}} = \overbrace{rP\left(1-\frac{P}{K}\right)}^{plant\ growth} - \overbrace{\frac{e_1PZ}{1+e_1h_1P+e_2h_2A}}^{plant\ loss} + \overbrace{d_{11}\nabla^2P}^{plant\ diffusion}, \\ \frac{\partial^{\alpha_2}Z}{\partial t^{\alpha_2}} = \underbrace{\frac{n_1e_1PZ+n_2e_2AZ}{1+e_1h_1P+e_2h_2A}}_{animal\ gain} - \underbrace{\tau Z}_{natural\ death} - \underbrace{\sigma\frac{PZ}{h+P}}_{animal\ death} + \underbrace{d_{21}\nabla^2P+d_{31}\nabla^2Z}_{plant\ and\ animal\ diffusion}, \end{cases} \tag{1.2}$$

where P and Z represent the population densities of phytoplankton and zooplankton, respectively, at time t. ∇^2 stands for the Laplacian operator of the two-dimensional plane, Ω is a bounded connected region with smooth boundaries $\partial\Omega$, and d_{11} and d_{31} represent the diffusion coefficients of phytoplankton

and zooplankton, respectively. These parameters characterize the stochastic movement of individuals within a population from areas of high concentration to those of lower density. d_{21} is a cross-diffusion coefficient that indicates the effect of the presence of phytoplankton on the movement of zooplankton populations. $\alpha_i (i = 1, 2)$ is the fractional-order orders, $0 < \alpha_i < 1$ and $\frac{\partial^{\alpha_1} P}{\partial t^{\alpha_1}}, \frac{\partial^{\alpha_2} Z}{\partial t^{\alpha_2}}$ are the Grünwald-Letnikov (GL) fractional derivative. t is the time variable. The meanings of the parameters in the model are shown in Table 1.

Table 1. Parameter and biological significance in the model.

Parameter	Ecological Significance
r	The intrinsic growth rate of phytoplankton
K	The carrying capacity of the environment for phytoplankton
h_1	The time zooplankton need to process one unit of phytoplankton
h_2	The time zooplankton need to process one unit of supplementary food
e_1	The capacity of zooplankton to prey on phytoplankton
e_2	The capacity of zooplankton to forage for supplementary food
n_1	The nutritional value of phytoplankton
n_2	The nutritional value of supplementary food
A	The biomass of supplementary food
τ	The mortality rate of zooplankton
σ	The proportion of toxins released by phytoplankton
h	The half-saturation constant

Several numerical schemes have been used to solve the Fractional-order reaction-diffusion equation, the Galerkin method [21, 22], the Fourier spectral method [23, 24], the finite difference method [25, 26], the operational matrix method [27, 28], and so on [29–34]. In this paper, we investigate dynamic properties and numerical solutions of the fractional-order PZEM (1.2). The major contributions of this paper are as follows:

(a) The concept of the phytoplankton-zooplankton ecological model is first extended to fractional-order PZEM that incorporates the effects of toxic substances and additional food transmission in the environment. This model leverages the memory effect of fractional-order derivatives to more effectively capture biological significance compared to traditional integer-order models.

(b) Stability, Turing instability, Hopf bifurcation, and weakly nonlinear property are analyzed for the PZEM. a new high-precision numerical method is developed for the fractional PZEM without diffusion term, and a discretization method is established for the PZEM with a diffusion term.

(c) Numerical simulations show some novel chaotic attractor and pattern dynamical behaviors of the PZEM.

The paper is organized as follows: In Section 2, we give the stability and Hopf bifurcation analysis. In Section 3, we detail weakly nonlinear analysis. In Section 4, we give the numerical algorithm and the numerical simulation results of the system. Finally, in Section 5, we the summarize paper.

2. Stability analysis

In this section, we investigate the stability of the equilibrium point and the emergence of Hopf bifurcation. Let

$$\bar{u} = e_1 h_1 P, \quad \bar{v} = \frac{e_1}{r} Z, \quad t = rT, \quad \kappa = e_1 h_1 K, \quad \alpha = \frac{n_1 h_2}{n_2 h_1},$$
$$\tau = \frac{n_1}{r h_1}, \quad \zeta = \frac{n_2 e_2 h_1}{n_1} A, \quad m = \frac{\tau}{r}, \quad \mu = \frac{\tau}{r}, \quad G = e_1 h h_1.$$

Equation (1.2) is converted to the following form:

$$\begin{cases} \frac{\partial^{\alpha_1}}{\partial t^{\alpha_1}} \bar{u} = \bar{u}\left(1 - \frac{\bar{u}}{\kappa}\right) - \frac{\bar{u}\bar{v}}{1+\alpha\zeta+\bar{u}} + d_1 \nabla^2 \bar{u}, \\ \frac{\partial^{\alpha_2}}{\partial t^{\alpha_2}} \bar{v} = \frac{\tau(\bar{u}+\zeta)\bar{v}}{1+\alpha\zeta+\bar{u}} - m\bar{v} - \mu \frac{\bar{u}\bar{v}}{G+\bar{u}} + d_2 \nabla^2 \bar{u} + d_3 \nabla^2 \bar{v}, \end{cases} \tag{2.1}$$

where, $d_1 = e_1 h_1 d_{11}, d_2 = e_1 h_1 d_{21}, d_3 = \frac{e_1}{r} d_{31}$.

2.1. Stability analysis

We analyze the stability of Eq (2.1) without the diffusion term.

$$\begin{cases} \frac{\partial^{\alpha_1}}{\partial t^{\alpha_1}} \bar{u} = \bar{u}\left(1 - \frac{\bar{u}}{\kappa}\right) - \frac{\bar{u}\bar{v}}{1+\alpha\zeta+\bar{u}}, \\ \frac{\partial^{\alpha_2}}{\partial t^{\alpha_2}} \bar{v} = \frac{\tau(\bar{u}+\zeta)\bar{v}}{1+\alpha\zeta+\bar{u}} - m\bar{v} - \mu \frac{\bar{u}\bar{v}}{G+\bar{u}}. \end{cases} \tag{2.2}$$

Solving the following equation:

$$\begin{cases} \bar{u}\left(1 - \frac{\bar{u}}{\kappa}\right) - \frac{\bar{u}\bar{v}}{1+\alpha\zeta+\bar{u}} = 0, \\ \frac{\tau(\bar{u}+\zeta)\bar{v}}{1+\alpha\zeta+\bar{u}} - m\bar{v} - \mu \frac{\bar{u}\bar{v}}{G+\bar{u}} = 0. \end{cases} \tag{2.3}$$

We can get the following equilibrium points of Eq (2.2):

$$E_0 = (0, 0), \quad E_1 = (\kappa, 0), \quad E^* = (\bar{u}^*, \bar{v}^*), \tag{2.4}$$

where

$$\bar{v}^* = (1 + \alpha\zeta + \bar{u}^*)\left(1 - \frac{\bar{u}^*}{\kappa}\right).$$

u^* represents the positive solution to the quadratic equation (2.5)

$$\bar{D}_1 \bar{u}^2 + \bar{D}_2 \bar{u} + \bar{D}_3 = 0, \tag{2.5}$$

where

$$\bar{D}_1 = \tau - m - \mu, \bar{D}_3 = \tau\zeta G - mG - m\alpha\zeta G, \bar{D}_2 = \tau\zeta + \tau G - m\alpha\zeta - mG - \mu\alpha\zeta - \mu - m.$$

Solving Eq (2.5), we can get:

$$\begin{cases} \bar{u}^*_{1,2} = \frac{-(\tau\zeta+\tau H-m\alpha\zeta-mH-\mu\alpha\zeta-\mu-m)}{2(\tau-m-\mu)} \pm \frac{\sqrt{(\tau\zeta+\tau H-m\alpha\zeta-mH-\mu\alpha\zeta-\mu-m)^2-4(\tau-m-\mu)(\tau\zeta H-mH-m\alpha\zeta H)}}{2(\tau-m-\mu)}, \\ \bar{v}^* = (1 + \alpha\zeta + \bar{u}^*)\left(1 - \frac{\bar{u}^*}{\kappa}\right). \end{cases} \tag{2.6}$$

The Jacobian matrix associated with $E^* = (\bar{u}^*, \bar{v}^*)$ is formulated as follows

$$J = \begin{bmatrix} a_{11} & a_{12} \\ a_{21} & a_{22} \end{bmatrix}, \tag{2.7}$$

where

$$a_{11} = 1 - \frac{2\bar{u}^*}{\kappa} - \frac{\bar{v}^*(1+\alpha\zeta)}{(1+\alpha\zeta+\bar{u}^*)^2},\ a_{12} = -\frac{\bar{u}^*}{1+\alpha\zeta+\bar{u}^*},$$
$$a_{21} = \frac{\tau\bar{v}^*(1+\alpha\zeta-\zeta)}{(1+\alpha\zeta+\bar{u}^*)^2} - \frac{\mu\bar{v}^*G}{(G+\bar{u}^*)^2},\ a_{22} = \frac{\tau(\bar{u}^*+\zeta)}{1+\alpha\zeta+\bar{u}^*} - m - \frac{\mu\bar{u}^*}{G+\bar{u}^*}.$$

When $(\alpha_1, \alpha_2) = (1, 1)$, the characteristic equation at the equilibrium point is as follows:

$$\lambda^2 + Tr_0\lambda + \triangle_0 = 0, \tag{2.8}$$

where,

$$Tr_0 = a_{11} + a_{22}, \triangle_0 = a_{11}a_{22} - a_{21}a_{12}.$$

Let $\alpha = 0.55, \tau = 4.1, \zeta = 0.72, G = 8.43, \mu = 0.79, \kappa = 2.38$, and $m = 2.45$. The system's equilibrium point and its associated eigenvalues are presented in Table 2.

Table 2. The calculation results of the equilibrium point, eigenvalue, and argument of the system.

Equilibrium point		Eigenvalues of Jacobian matrix		Stability
0	0	–0.3354	1	Unstability
2.3800	0	–1	0.7421	Unstability
0.3131	1.4843	0.0138–0.4838i	0.0138+0.4838i	Unstability

It can be seen from Table 3 that all three equilibrium points are unstable points, and the system may generate chaos. Next, we introduce a high-precision numerical method for numerical simulation.

Table 3. Comparison of methods for problem (2.9) when $\beta = 0.9$ and $t \in [0, 1]$.

Method	$\alpha = 0.4$		$\alpha = 0.7$		$\alpha = 1$	
	$h = 0.01$	$h = 0.05$	$h = 0.01$	$h = 0.05$	$h = 0.01$	$h = 0.05$
Closed-from solution [35]	3.2307e-02	5.4302e-02	4.5734e-02	2.5713e-01	2.0716e-01	4.5136e-01
Present method	8.9463e-05	5.6724e-04	9.1684e-05	7.3524e-04	2.1527e-04	4.5136e-03

2.2. Numerical comparison

In simulations of this section, let $\alpha = 1.1, \tau = 4.4, \zeta = 0.8, G = 8, n = 1.75, \kappa = 5.3$, and $m = 2.5$ and initial conditions $u_0 = 1$ and $v_0 = 1$. We set the time step size $h = 0.01$ and the time as $T = 600$ for simulation. Figure 1 shows numerical results at $(\alpha_1, \alpha_2) = (0.895, 0.994)$.

We consider the following fractional order GL initial value problem

$$\begin{cases} D_t^\alpha y(t) = t^\beta, \\ y(0) = 0. \end{cases} \tag{2.9}$$

Numerical simulations are performed for Eq (2.9). Compared with the closed-from solution, the simulation results of the high-precision numerical method are in good agreement with the simulation results of other methods, and the accuracy is higher. This verifies the effectiveness of the high-precision numerical method.

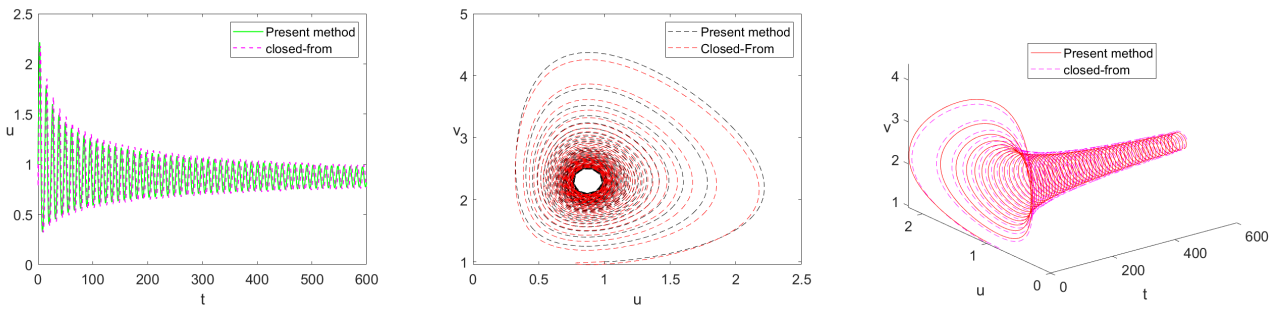

(a) Time series plots (b) $u-v$ phase diagram (c) phase diagram

Figure 1. Comparative numerical result of the two methods of the model $(\alpha, \tau, \zeta, G, n, \kappa, m) = (1.1, 4.4, 0.8, 8, 1.75, 5.3, 2.5)$, $\alpha_1 = 0.895$, and $\alpha_2 = 0.994$.

2.3. *Brief description of the numerical methodology*

We first consider the following GL differential equation:

$$\frac{d^\alpha}{dt^\alpha} y(t) = f(t, y(t)). \tag{2.10}$$

According to [36], we can get the high-precision numerical method [36–39]:

$$y(t_k) = h^\alpha f(t_k, y(t_{k-1})) - \sum_{i=1}^{m} \vartheta_j^{(\alpha,p)} y\left(t_{k-j}\right), \tag{2.11}$$

where,

$$\begin{cases} \vartheta_0^{(\alpha,p)} = \mathbf{g}_0, k = 0, \\ \vartheta_k^{(\alpha,p)} = -\frac{1}{\mathbf{g}_0} \sum_{i=0}^{k-1} (1 - i\frac{1+\alpha}{k}) \mathbf{g}_i \vartheta_{k-i}^{(\alpha,p)}, k = 1, 2, ..., p-1, \\ \vartheta_k^{(\alpha,p)} = -\frac{1}{\mathbf{g}_0} \sum_{i=0}^{p} (1 - i\frac{1+\alpha}{k}) \mathbf{g}_i \vartheta_{k-i}^{(\alpha,p)}, k = p, p+1, p+2, ... \end{cases} \tag{2.12}$$

$$\begin{pmatrix} \mathbf{g}_0 \\ \mathbf{g}_1 \\ \mathbf{g}_2 \\ \vdots \\ \mathbf{g}_p \end{pmatrix} = -\begin{pmatrix} 1 & 1 & 1 & \cdots & 1 \\ 1 & 2 & 3 & \cdots & p+1 \\ 1 & 2^2 & 3^2 & \cdots & (p+1)^2 \\ \vdots & \vdots & \vdots & \cdots & \vdots \\ 1 & 2^p & 3^p & \cdots & (p+1)^p \end{pmatrix}^{-1} \begin{pmatrix} 0 \\ 1 \\ 2 \\ \vdots \\ p \end{pmatrix}. \tag{2.13}$$

Where $m = [t_k/h] + 1$, h is the step size. Therefore, a high-precision numerical method for the system (2.2) is the following

$$\begin{cases} \bar{u}_k = h^{\alpha_1} \left(\bar{u}_{k-1} \left(1 - \frac{\bar{u}_{k-1}}{\kappa}\right) - \frac{\bar{u}_{k-1}\bar{v}_{k-1}}{1+\alpha\zeta+\bar{u}_{k-1}} \right) + \bar{u}_0 - \sum_{j=1}^{m} \vartheta_j^{(\alpha_1,p)} \bar{u}_{k-j}, \\ \bar{v}_k = h^{\alpha_2} \left(\frac{\tau(\bar{u}_k+\zeta)\bar{v}_{k-1}}{1+\alpha\zeta+\bar{u}_k} - m\bar{v}_{k-1} - \mu\frac{\bar{u}_k\bar{v}_{k-1}}{G+\bar{u}_k} \right) + \bar{v}_0 - \sum_{j=1}^{m} \vartheta_j^{(\alpha_2,p)} \bar{v}_{k-j}. \end{cases} \tag{2.14}$$

According to [36, 40], the least common order of the system is identified as 0.9819. Let $(\alpha_1, \alpha_2) = (1.05, 0.95), \alpha = 0.55, \tau = 4.1, \zeta = 0.72, G = 8.43, \mu = 0.79, \kappa = 2.38$, and $m = 2.45$, and the characteristic equation of the system is given by

$$\lambda^{40} - \frac{10667}{28823}\lambda^{21} - \frac{24789}{90071}\lambda^{19} + \frac{1039692}{4437077} = 0, \tag{2.15}$$

with characteristic roots $\lambda_{1,2} = 1.0358 \pm 0.0439i$, as $|arg(\lambda_{1,2})| = 0.0423 < \frac{\pi}{40}$. This indicates that the instability of the system may generate chaos. It can be seen from Figure 2 that the system generates chaos. The chaotic phenomenon of the system gradually disappears over time and tends to a stable state.

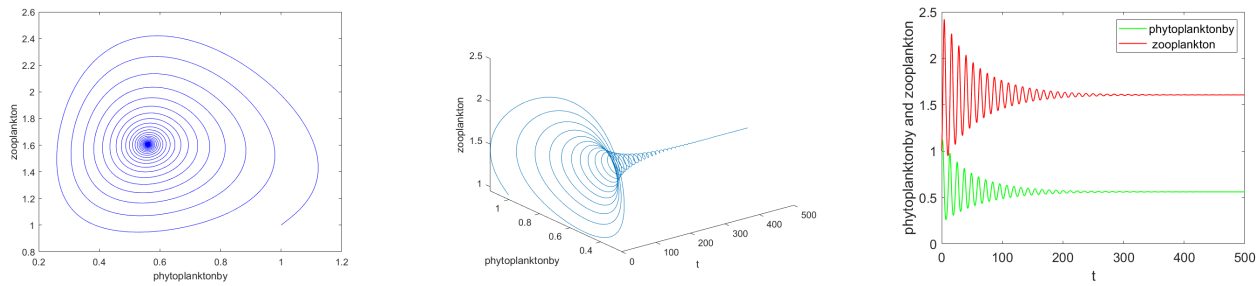

Figure 2. Numerical simulation of phase diagrams and time series plot of system (2.2) at $(\alpha_1, \alpha_2) = (1.05, 0.95)$.

We set different orders $(\alpha_1, \alpha_2) = (1.1, 0.95)$ to observe the influence of the order on the dynamic behavior of the system at parameters $\alpha = 0.55, \tau = 4.1, \zeta = 0.72, G = 8.43, n = 0.79$, $\kappa = 2.38$, and $m = 2.45$. The characteristic equation of the system is given by

$$\lambda^{41} - \frac{10667}{28823}\lambda^{22} - \frac{24789}{90071}\lambda^{19} + \frac{1039692}{4437077} = 0, \tag{2.16}$$

with characteristic roots $\lambda_{1,2} = 1.0021 \pm 0.2687i$, as $|arg(\lambda_{1,2})| = 0.2620 < \frac{\pi}{40}$. It indicates that the instability of the system may generate chaos. It can be seen from Figure 3 that the system is in a quasi-periodic state.

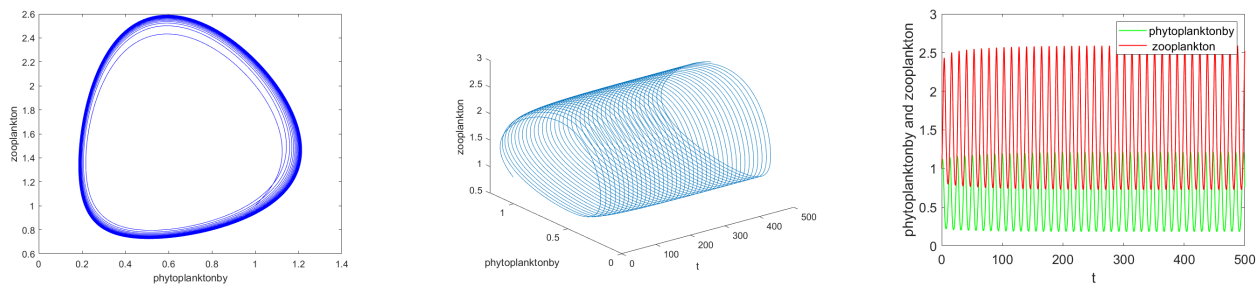

Figure 3. Numerical simulation of phase diagrams and time series plot of system (2.2) at $(\alpha_1, \alpha_2) = (1.1, 0.95)$.

To gain a clearer view of the system's dynamic behavior, Figure 4 shows the phase diagram of the system under different α orders.

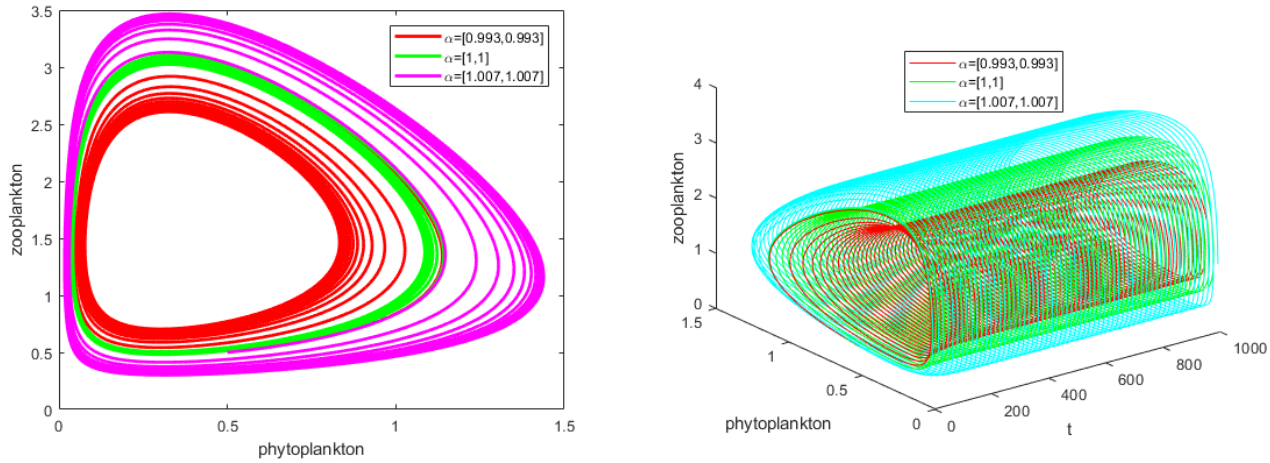

Figure 4. Comparison of the phytoplankton-zooplankton phase diagram of the system (2.2) at different fractional-order derivatives.

2.4. *Hopf bifurcation analysis*

Next, we explore the potential for a Hopf bifurcation at E^*. A Hopf bifurcation is critical as it marks a transition in the model's stability and the emergence of periodic solutions. To achieve this, the characteristic roots of system (2.2) must be purely complex.

The solution to system (2.2) is obtained as follows:

$$\lambda_{1,2} = \frac{Tr_0 \pm \sqrt{Tr_0^2 - 4det_0}}{2}. \tag{2.17}$$

When $\alpha = 1$, system (2.2) undergoes a destabilizing Hopf bifurcation under the conditions $tr_0 = 0$ and $det_0 > 0$. Given that the stability of system (2.2) is influenced by the fractional derivative, this derivative can be considered a parameter in the Hopf bifurcation. We now determine the conditions for the Hopf bifurcation for system (2.2) around parameter E_*, $\alpha = \alpha_h$:

(1) At the equilibrium point E_*, the Jacobian matrix possesses a pair of complex conjugate eigenvalues $\lambda_{1,2} = a_i + ib_i$, which transition to being purely imaginary at $\alpha = \alpha_h$;

(2) $m(\alpha_h) = 0$ where $m(\alpha) = \alpha\frac{\pi}{2} - \min\limits_{1\le i\le 2}|arg(\lambda_i)|$;

(3) $\frac{\partial m(\alpha)}{\partial \alpha}\Big|_{\alpha=\alpha_h} \neq 0$.

We now demonstrate that E_* experiences a Hopf bifurcation as α crosses the value α_h.

Proof. Given that $tr_0^2 - 4\det_0 < 0$ and $tr_0 > 0$, the eigenvalues form a complex conjugate pair with a positive real component. Thus,

$$0 < arg(\lambda_{12}) = \tan^{-1}\left(\frac{\sqrt{4\det_0 - tr_0^2}}{tr_0}\right) < \frac{\pi}{2}, \tag{2.18}$$

and $\alpha\frac{\pi}{2} > \left|\tan^{-1}\left(\frac{\sqrt{4\det_0 - tr_0^2}}{tr_0}\right)\right|$ for some α. Let $\alpha_h\frac{\pi}{2} = \left|\tan^{-1}\left(\frac{\sqrt{4\det_0 - tr_0^2}}{tr_0}\right)\right|$, get $\alpha_h = \frac{2}{\pi}\tan^{-1}\left(\frac{\sqrt{4\det_0 - tr_0^2}}{tr_0}\right)$. Moreover, $\frac{\partial m(\alpha)}{\partial \alpha}\Big|_{\alpha=\alpha_h} = \frac{\pi}{2} \neq 0$. Therefore, all Hopf conditions satisfy.

3. Weakly nonlinear analysis

Above, we analyze the dynamical behavior of fractional system (2.2). The expression of the solution of system (2.1) involves more complex special functions, such as the Mittag-Leffler function and other hypergeometric functions. Although the form of the solution exists, its expression is very large. Therefore, in this section, we reveal various spatiotemporal behaviors around the Turing bifurcation threshold d_2 and derive the amplitude equations associated with system (2.1) at $\alpha_1 = \alpha_2 = 1$ using multi-scale and weakly nonlinear analysis. The solution of system (2.1) is written in the following form:

$$\begin{pmatrix} \bar{u} \\ \bar{v} \end{pmatrix} = \begin{pmatrix} \bar{u}^* \\ \bar{v}^* \end{pmatrix} + \sum_{j=1}^{3} \begin{pmatrix} A_j^{\bar{u}^*} \\ A_j^{\bar{v}^*} \end{pmatrix} e^{iq_j \cdot r} + \text{ c.c.}, \tag{3.1}$$

where $\left(A_j^{\bar{u}^*}, A_j^{\bar{v}^*}\right)^T$ represents the magnitude of the wave vector $\boldsymbol{q}_j$, fulfilling the condition that $\left|\boldsymbol{q}_j\right| = q_T$.

Adding a perturbation to the equilibrium point $E^*(u^*, v^*)$, such that $\bar{u} = \bar{u}^* + u$, $\bar{v} = \bar{v}^* + v$, and substituting them into system (2.1), and performing a Taylor expansion, we can get the following form:

$$\begin{cases} \frac{\partial u}{\partial t} = a_{11}u + a_{12}v + k_{20}u^2 + k_{02}v^2 + k_{11}uv + k_{30}u^3 + k_{03}v^3 + k_{21}u^2v + k_{12}uv^2 + d_1\nabla^2 u, \\ \frac{\partial v}{\partial t} = a_{11}u + a_{22}v + m_{20}u^2 + m_{02}v^2 + m_{11}uv + m_{30}u^3 + m_{03}v^3 + m_{21}u^2v + m_{12}uv^2 + d_2\nabla^2 u + d_3\nabla^2 v, \end{cases} \tag{3.2}$$

where

$$\begin{gathered} k_{02} = 0, \quad k_{03} = 0, \quad k_{12} = 0, \quad m_{02} = 0, \quad m_{03} = 0, \quad m_{12} = 0, \\ k_{11} = -\frac{1+\alpha\zeta}{(1+\alpha\zeta+\bar{u}^*)^2}, \quad m_{11} = \frac{(1+\alpha\zeta-\zeta)\tau}{(1+\alpha\zeta+\bar{u}^*)^2} - \frac{\mu G}{(G+\bar{u}^*)^2}, \\ k_{21} = -\frac{1+\alpha\zeta}{(1+\alpha\zeta+\bar{u}^*)^3}, \quad m_{21} = \frac{-\tau(1+\alpha\zeta-\zeta)}{(1+\alpha\zeta+\bar{u}^*)^3} + \frac{\mu G}{(G+\bar{u}^*)^3}, \\ k_{30} = -\frac{(1+\alpha\zeta)\left(1-\frac{\bar{u}^*}{\kappa}\right)}{(1+\alpha\zeta+\bar{u}^*)^3}, \quad m_{30} = \frac{\tau\left(1-\frac{\bar{u}^*}{\kappa}\right)(1+\alpha\zeta-\zeta)}{(1+\alpha\zeta+\bar{u}^*)^3} - \frac{\mu G\bar{v}^*}{(G+\bar{u}^*)^4}, \\ k_{20} = -\frac{1}{\kappa} + \frac{(1+\alpha\zeta)\left(1-\frac{\bar{u}^*}{\kappa}\right)}{(1+\alpha\zeta+\bar{u}^*)^2}, \quad m_{20} = \frac{-\tau(1+\alpha\zeta-\zeta)\left(1-\frac{\bar{u}^*}{\kappa}\right)}{(1+\alpha\zeta+\bar{u}^*)^2} + \frac{\mu G\bar{v}^*}{(G+\bar{u}^*)^3}. \end{gathered}$$

Let $U = (u, v)^T$ and system (3.2) can be simplified as

$$\frac{\partial U}{\partial t} = LU + N(U, U), \tag{3.3}$$

$$L = \begin{pmatrix} a_{11} + d_1\nabla^2 & a_{12} \\ a_{21} + d_2\nabla^2 & a_{22} + d_3\nabla^2 \end{pmatrix},$$

where

$$N = \begin{pmatrix} k_{20}u^2 + k_{02}v^2 + k_{11}uv + k_{30}u^3 + k_{03}v^3 + k_{21}u^2v + k_{12}uv^2 \\ m_{20}u^2 + m_{02}v^2 + m_{11}uc + m_{30}u^3 + m_{03}v^3 + m_{21}u^2v + m_{12}uv^2 \end{pmatrix}.$$

Here, L denotes a linear operator and N represents a nonlinear operator.

We expand parameter d_2 with a sufficiently small parameter ε, so we can obtain:

$$d_2^T = \varepsilon d_2^{(1)} + \varepsilon^2 d_2^{(2)} + \varepsilon^3 d_2^{(3)} + O\left(\varepsilon^3\right). \tag{3.4}$$

We develop variable U and nonlinear term N, respectively, the small parameter ε:

$$U = \begin{pmatrix} u \\ v \end{pmatrix} = \varepsilon \begin{pmatrix} u_1 \\ v_1 \end{pmatrix} + \varepsilon^2 \begin{pmatrix} u_2 \\ v_2 \end{pmatrix} + \varepsilon^3 \begin{pmatrix} u_3 \\ v_3 \end{pmatrix} + O\left(\varepsilon^3\right), \tag{3.5}$$

$$N = \varepsilon^2 N_2 + \varepsilon^3 N_3 + O\left(\varepsilon^4\right), \tag{3.6}$$

where

$$N_2 = \begin{pmatrix} k_{20}u_1^2 + k_{11}u_1v_1 \\ m_{20}u_1^2 + m_{11}u_1v_1 \end{pmatrix},$$
$$N_3 = \begin{pmatrix} 2k_{20}u_1u_2 + k_{11}u_1v_2 + k_{11}u_2v_1 + k_{30}u_1^3 + k_{21}u_1^2v_1 \\ 2m_{20}u_1u_2 + m_{11}u_1v_2 + m_{11}u_2v_1 + m_{30}u_1^3 + m_{21}u_1^2v_1 \end{pmatrix}.$$

We decompose operator L into the following form:

$$L = L_c + \left(d_2 - d_2^T\right) M, \tag{3.7}$$

where

$$L_c = \begin{pmatrix} d_1\nabla^2 + a_{11} & a_{12} \\ d_2^T\nabla^2 + a_{21} & d_3\nabla^2 + a_{22} \end{pmatrix}, M = \begin{pmatrix} b_{11} & b_{12} \\ b_{21} & b_{22} \end{pmatrix}.$$

Using the multiple-scale approach, we differentiate the system's time scales into $T_1 = \varepsilon t, T_2 = \varepsilon^2 t, T_3 = \varepsilon^3 t$, which are mutually independent. Consequently, the time derivative can be articulated as:

$$\frac{\partial}{\partial t} = \varepsilon \frac{\partial}{\partial T_1} + \varepsilon^2 \frac{\partial}{\partial T_2} + \varepsilon^3 \frac{\partial}{\partial T_3} + O\left(\varepsilon^3\right). \tag{3.8}$$

Substituting Eqs (3.4)–(3.8) into Eq (3.3), we can obtain the following equation:

$$\varepsilon : L_c \begin{pmatrix} u_1 \\ v_1 \end{pmatrix} = 0, \tag{3.9}$$

$$\varepsilon^2 : L_c \begin{pmatrix} u_2 \\ v_2 \end{pmatrix} = \frac{\partial}{\partial T_1} \begin{pmatrix} u_1 \\ v_1 \end{pmatrix} - d_2^{(1)} M \begin{pmatrix} u_1 \\ v_1 \end{pmatrix} - N_2, \tag{3.10}$$

$$\varepsilon^3 : L_c \begin{pmatrix} u_3 \\ v_3 \end{pmatrix} = \frac{\partial}{\partial T_1} \begin{pmatrix} u_2 \\ v_2 \end{pmatrix} + \frac{\partial}{\partial T_2} \begin{pmatrix} u_1 \\ v_1 \end{pmatrix} - d_2^{(1)} M \begin{pmatrix} u_2 \\ v_2 \end{pmatrix} - d_2^{(2)} M \begin{pmatrix} u_1 \\ v_1 \end{pmatrix} - N_3. \tag{3.11}$$

The 1st order of $(O(\varepsilon))$:

$$L_c\begin{pmatrix} u_1 \\ v_1 \end{pmatrix} = 0. \tag{3.12}$$

The solution of Eq (3.12) is

$$\begin{pmatrix} u_1 \\ v_1 \end{pmatrix} = \begin{pmatrix} \varphi \\ 1 \end{pmatrix} \sum_{j=1}^{3} \left(W_j e^{i\boldsymbol{q}_j \cdot r}\right) + c.c., \tag{3.13}$$

where $\varphi = \frac{-a_{12}}{a_{11}-d_1 q_c^2}, \left|\boldsymbol{q}_j\right| = q_c, q_c = q_T\left(d_2^T\right)$. Additionally, W_j denotes the amplitude of $e^{i\boldsymbol{q}_j \cdot r}$.

The 2nd order of $(O\left(\varepsilon^2\right))$:

$$L_c\begin{pmatrix} u_2 \\ v_2 \end{pmatrix} = \frac{\partial}{\partial T_1}\begin{pmatrix} u_1 \\ v_1 \end{pmatrix} - d_2^{(1)} M\begin{pmatrix} u_1 \\ v_1 \end{pmatrix} - N_2 = \begin{pmatrix} F_u \\ F_v \end{pmatrix}, \tag{3.14}$$

F_u^j and $F_v^j (j = 1, 2, 3)$ are the coefficients with respect to $e^{i\boldsymbol{q}_j \cdot r}$ in F_u and F_v, respectively.

Using the Fredholm solvability condition for Eq (3.14), the vector function on the right-hand side must be perpendicular to the zero eigenvalue of L_c^+. The zero eigenvector of L_c is:

$$\begin{pmatrix} 1 \\ \psi \end{pmatrix} e^{-iq_j r} + c.c., \ j = 1, 2, 3, \tag{3.15}$$

with $\psi = -\frac{a_{11}-d_1 q_c^2}{a_{21}-d_2^T q_c^2}$. From the orthogonal condition:

$$(1, \psi)\begin{pmatrix} F_u^j \\ F_v^j \end{pmatrix} = 0, \ j = 1, 2, 3. \tag{3.16}$$

Utilizing the Fredholm solvability condition as stated in Eq (3.16), we arrive at the following:

$$\begin{cases} (\varphi + \psi)\frac{\partial W_1}{\partial T_1} = d_2^{(1)}\eta_0 W_1 + 2(\eta_1 + \psi\eta_2)\overline{W}_2\overline{W}_3, \\ (\varphi + \psi)\frac{\partial W_2}{\partial T_1} = d_2^{(1)}\eta_0 W_2 + 2(\eta_1 + \psi\eta_2)\overline{W}_1\overline{W}_3, \\ (\varphi + \psi)\frac{\partial W_3}{\partial T_1} = d_2^{(1)}\eta_0 W_3 + 2(\eta_1 + \psi\eta_2)\overline{W}_1\overline{W}_2, \end{cases} \tag{3.17}$$

where

$$\begin{cases} \eta_0 = (\varphi b_{11} + b_{22}) + \psi(\varphi b_{21} + b_{22}), \\ \eta_1 = \frac{1}{2}k_{20}\varphi^2 + k_{11}\varphi, \\ \eta_2 = \frac{1}{2}m_{20}\varphi^2 + m_{11}\varphi. \end{cases}$$

Next, higher-order disturbance terms are introduced:

$$\begin{pmatrix} u_2 \\ v_2 \end{pmatrix} = \begin{pmatrix} U_0 \\ V_0 \end{pmatrix} + \sum_{j=1}^{3}\begin{pmatrix} U_j \\ V_j \end{pmatrix} e^{i\boldsymbol{q}_j \cdot r} + \sum_{j=1}^{3}\begin{pmatrix} U_{jj} \\ V_{jj} \end{pmatrix} e^{2i\boldsymbol{q}_j \cdot r} + \tag{3.18}$$
$$\begin{pmatrix} U_{12} \\ V_{12} \end{pmatrix} e^{i(\boldsymbol{q}_1 - \boldsymbol{q}_2)\cdot r} + \begin{pmatrix} U_{23} \\ V_{23} \end{pmatrix} e^{i(\boldsymbol{q}_2 - \boldsymbol{q}_3)\cdot r} + \begin{pmatrix} U_{31} \\ V_{31} \end{pmatrix} e^{i(\boldsymbol{q}_3 - \boldsymbol{q}_1)\cdot r} + c.c..$$

We substitute formulas (3.13) and (3.18) into formula (3.10). By solving the equations corresponding to different modes, it is known that the coefficients have the following forms:

$$\begin{pmatrix} U_0 \\ V_0 \end{pmatrix} = \begin{pmatrix} u_{00} \\ v_{00} \end{pmatrix} \left(|W_1|^2 + |W_2|^2 + |W_3|^2\right), \; U_j = \varphi Y_j,$$
$$\begin{pmatrix} U_{jj} \\ V_{jj} \end{pmatrix} = \begin{pmatrix} u_{11} \\ v_{11} \end{pmatrix} W_j^2, \; \begin{pmatrix} U_{ij} \\ V_{ij} \end{pmatrix} = \begin{pmatrix} \bar{u}^* \\ \bar{v}^* \end{pmatrix} W_i \overline{W_j},$$

where

$$\begin{pmatrix} \bar{u}_{00} \\ \bar{v}_{00} \end{pmatrix} = \frac{-2}{a_{11}a_{22}-a_{21}a_{12}} \begin{pmatrix} a_{22}\eta_1 - a_{12}\eta_2 \\ a_{11}\eta_2 - a_{21}\eta_1 \end{pmatrix}, \tag{3.19}$$

$$\begin{pmatrix} \bar{u}_{11} \\ \bar{v}_{11} \end{pmatrix} = \begin{pmatrix} \frac{a_{12}\eta_2-(a_{22}-4d_3q_c^2)\eta_1}{(a_{11}-4d_1q_c^2)(a_{22}-4d_3q_c^2)-(a_{21}-4d_2^Tq_c^2)a_{12}} \\ \frac{(a_{21}-4d_2^Tq_c^2)\eta_1-(a_{11}-4d_1q_c^2)\eta_2}{(a_{11}-4d_1q_c^2)(a_{22}-4d_3q_c^2)-(a_{21}-4d_2^Tq_c^2)a_{12}} \end{pmatrix}, \tag{3.20}$$

$$\begin{pmatrix} \bar{u}_* \\ \bar{v}_* \end{pmatrix} = 2\begin{pmatrix} \frac{a_{12}\eta_2-(a_{22}-3d_3q_c^2)\eta_1}{(a_{11}-3d_1q_c^2)(a_{22}-3d_3q_c^2)-(a_{21}-3d_2^Tq_c^2)a_{12}} \\ \frac{(a_{21}-3d_2^Tq_c^2)\eta_1-(a_{11}-3d_1q_c^2)\eta_2}{(a_{11}-3d_1q_c^2)(a_{22}-3d_3q_c^2)-(a_{21}-3d_2^Tq_c^2)a_{12}} \end{pmatrix}. \tag{3.21}$$

From the orthogonal condition, we obtain:

$$\begin{cases} (\varphi+\psi)\left(\frac{\partial Y_1}{\partial T_1}+\frac{\partial W_1}{\partial T_2}\right) = \eta_0\left(d_2^{(2)}W_1 + d_2^{(1)}Y_1\right) - \left[(Q_1+\psi R_1)|W_1|^2 + (Q_2+\psi R_2)\left(|W_2|^2+|W_3|^2\right)\right]W_1 \\ \qquad +2(\eta_1+\psi\eta_2)\left(\overline{W_2Y_3}+\overline{W_3Y_2}\right), \\ (\varphi+\psi)\left(\frac{\partial Y_2}{\partial T_1}+\frac{\partial W_2}{\partial T_2}\right) = \eta_0\left(d_2^{(2)}W_2 + d_2^{(1)}Y_2\right) - \left[(Q_1+\psi R_1)|W_2|^2 + (Q_2+\psi R_2)\left(|W_1|^2+|W_3|^2\right)\right]W_2 \\ \qquad +2(\eta_1+\psi\eta_2)\left(\overline{W_1Y_3}+\overline{W_3Y_1}\right), \\ (\varphi+\psi)\left(\frac{\partial Y_3}{\partial T_1}+\frac{\partial W_3}{\partial T_2}\right) = \eta_0\left(d_2^{(2)}W_3 + d_2^{(1)}Y_3\right) - \left[(Q_1+\psi R_1)|W_3|^2 + (Q_2+\psi R_2)\left(|W_2|^2+|W_1|^2\right)\right]W_3 \\ \qquad +2(\eta_1+\psi\eta_2)\left(\overline{W_2Y_1}+\overline{W_1Y_2}\right), \end{cases} \tag{3.22}$$

where

$$\begin{aligned} Q_1 &= -(2\varphi k_{20}+k_{11})(u_{00}+u_{11}) - \varphi k_{11}(v_{00}+v_{11}) - 3k_{30}\varphi^3 - 3k_{21}\varphi^2, \\ Q_2 &= -(2\varphi k_{20}+k_{11})(u_{00}+u_*) - \varphi k_{11}(v_{00}+v_*) - 6k_{30}\varphi^3 - 6k_{21}\varphi^2, \\ R_1 &= -(2\varphi m_{20}+m_{11})(u_{00}+u_{11}) - \varphi m_{11}(v_{00}+v_{11}) - 3m_{30}\varphi^3 - 3m_{21}\varphi^2, \\ R_2 &= -(2\varphi m_{20}+m_{11})(u_{00}+u_*) - \varphi m_{11}(v_{00}+v_*) - 6m_{30}\varphi^3 - 6m_{21}\varphi^2. \end{aligned}$$

The amplitude A_j is the coefficient of $e^{i\boldsymbol{q}_j\cdot r}$ at each level, so

$$A_j = \varepsilon W_j + \varepsilon^2 Y_j + O\left(\varepsilon^3\right). \tag{3.23}$$

Substituting Eqs (3.17) and (3.22) into Eq (3.23), we get the following amplitude equations:

$$\begin{cases} \tau_0\frac{\partial Z_1}{\partial t} = \eta Z_1 + \chi\bar{Z}_2\bar{Z}_3 - \left[g_1|Z_1|^2 + g_2\left(|Z_2|^2+|Z_3|^2\right)\right]Z_1, \\ \tau_0\frac{\partial Z_2}{\partial t} = \eta Z_2 + \chi\bar{Z}_1\bar{Z}_3 - \left[g_1|Z_2|^2 + g_2\left(|Z_1|^2+|Z_3|^2\right)\right]Z_2, \\ \tau_0\frac{\partial Z_3}{\partial t} = \eta Z_3 + \chi\bar{Z}_1\bar{Z}_2 - \left[g_1|Z_3|^2 + g_2\left(|Z_1|^2+|Z_2|^2\right)\right]Z_3, \end{cases} \tag{3.24}$$

where

$$\eta = \frac{d_2 - d_2^T}{d_2^T},$$
$$\tau_0 = \frac{\varphi + \psi}{d_2^T\left[(\varphi b_{11} + b_{12}) + \psi(\varphi b_{21} + b_{22})\right]},$$
$$\chi = \frac{k_{20}\varphi^2 + 2k_{11}\varphi + m_{20}\varphi^2\psi + 2m_{11}\varphi\psi}{d_2^T\left[(\varphi b_{11} + b_{12}) + \psi(\varphi b_{21} + b_{22})\right]},$$
$$g_1 = \frac{Q_1 + \psi R_1}{d_2^T\left[(\varphi b_{11} + b_{12}) + \psi(\varphi b_{21} + b_{22})\right]},$$
$$g_2 = \frac{Q_2 + \psi R_2}{d_2^T\left[(\varphi b_{11} + b_{12}) + \psi(\varphi b_{21} + b_{22})\right]}.$$

Since each amplitude $A_j = \omega_j e^{i\theta_j}$ $(j = 1, 2, 3)$ in Eq (3.24) can be decomposed into mode $\omega_j = |A_j|$ and phase angle θ_j, substituting A_j into Eq (3.24) to separate the real and imaginary parts yields the following equation:

$$\begin{cases} \tau_0 \frac{\partial\theta}{\partial t} = -\chi \frac{\omega_1^2\omega_2^2 + \omega_1^2\omega_3^2 + \omega_2^2\omega_3^2}{\omega_1\omega_2\omega_3} \sin\theta, \\ \tau_0 \frac{\partial\omega_1}{\partial t} = \eta\omega_1 + \chi\omega_2\omega_3\cos\theta - \left[g_1\omega_1^3 + g_2\left(\omega_2^2 + \omega_3^2\right)\omega_1\right], \\ \tau_0 \frac{\partial\omega_1}{\partial t} = \eta\omega_1 + \chi\omega_2\omega_3\cos\theta - \left[g_1\omega_1^3 + g_2\left(\omega_2^2 + \omega_3^2\right)\omega_1\right], \\ \tau_0 \frac{\partial\omega_1}{\partial t} = \eta\omega_1 + \chi\omega_2\omega_3\cos\theta - \left[g_1\omega_1^3 + g_2\left(\omega_2^2 + \omega_3^2\right)\omega_1\right], \end{cases} \tag{3.25}$$

where, $\theta = \theta_1 + \theta_2 + \theta_3$. From Eq (3.25), it can be deduced that the solution is stable under the conditions $\chi > 0, \psi = 0$ and $\chi < 0, \psi = \pi$. The solutions of Eq (3.25) are shown in Table 4.

Table 4. The relationship between pattern shape and steady-state solutions.

Conditions	Solution	Pattern shape
—	$\omega_1 = \omega_2 = \omega_3 = 0$	Stationary state
—	$\omega_1 = \sqrt{\frac{\eta}{g_1}}, \omega_2 = \omega_3 = 0$	Strip pattern
$\eta > \eta_1 = \frac{-\chi^2}{4(g_1 + 2g_2)}$	$\omega_1 = \omega_2 = \omega_3 = \frac{\lvert\chi\rvert \pm \sqrt{\chi^2 + 4(g_1 + 2g_2)\eta}}{2(g_1 + 2g_2)}$	Hexagon pattern
$g_2 > g_1, \eta > g_1\omega_1^2$	$\omega_1 = \frac{\lvert\chi\rvert}{g_2 - g_1}, \omega_2 = \omega_3 = \sqrt{\frac{\eta - g_1\omega_1^2}{g_1 + g_2}}$	Mixed state

4. Numerical simulation

In this section, we conduct numerical simulations to verify the theoretical analysis and observe its pattern dynamic behavior. In order to observe the dynamic behavior, we introduce the numerical method of the PZEM model (2.1). If $0 < \alpha_i < 1 (i = 1, 2)$, the time derivative is expressed by formula (2.11), and the space derivative is expressed by the following formula (4.2). If $\alpha_i = 1 (i = 1, 2)$, we employ the Euler discretization approach for conducting numerical simulations in

a two-dimensional domain $\Omega = [0, L_x] \times \left[0, L_y\right]$. We select $L_x = 250, L_y = 250$, a time increment $\Delta t = 0.2$, and a spatial increment $\Delta h = 0.69$. We denote $u_{pq}^n = u\left(x_p, y_q, n\Delta t\right)$ and $v_{pq}^n = v\left(x_p, y_q, n\Delta t\right)$. The model (2.1) is discretized using the Euler method, as outlined below:

$$\begin{cases} \frac{\bar{u}_{pq}^{n+1} - \bar{u}_{pq}^n}{\Delta t} = \bar{u}_{pq}^n \left(1 - \frac{\bar{u}_{pq}^n}{\kappa}\right) - \frac{\bar{u}_{pq}^n \bar{v}_{pq}^n}{1+\alpha\zeta+\bar{u}_{pq}^n} + d_1 \nabla^2 \bar{u}_{pq}^n, \\ \frac{\bar{v}_{pq}^{n+1} - \bar{v}_{pq}^n}{\Delta t} = \frac{\tau\left(\bar{u}_{pq}^n + \zeta\right)\bar{v}_{pq}^n}{1+\alpha\zeta+\bar{u}_{pq}^n} - m\bar{v}_{pq}^n - \mu \frac{\bar{u}_{pq}^n \bar{v}_{pq}^n}{G+\bar{u}_{pq}^n} + d_2 \nabla^2 \bar{u}_{pq}^n + d_3 \nabla^2 \bar{v}_{pq}^n, \end{cases} \tag{4.1}$$

where

$$\begin{cases} \nabla^2 \bar{u}_{pq} = \frac{\bar{u}_{p+1,q+1} + \bar{u}_{p-1,q-1} + \bar{u}_{p+1,q-1} + \bar{u}_{p-1,q+1} + 4\left(\bar{u}_{p+1,q} + \bar{u}_{p-1,q} + \bar{u}_{p,q+1} + \bar{u}_{p,q-1}\right) - 20\bar{u}_{pq}}{6h^2}, \\ \nabla^2 \bar{v}_{pq} = \frac{\bar{v}_{p+1,q+1} + \bar{v}_{p-1,q-1} + \bar{v}_{p+1,q-1} + \bar{v}_{p-1,q+1} + 4\left(\bar{v}_{p+1,q} + \bar{v}_{p-1,q} + \bar{v}_{p,q+1} + \bar{v}_{p,q-1}\right) - 20\bar{v}_{pq}}{6h^2}. \end{cases} \tag{4.2}$$

Next, we select the parameters shown in Table 5 and use Eq (4.1) to conduct numerical simulations.

Table 5. Parameter values.

α	τ	ζ	G	n	κ	m	κ_c	d_1	d_2	d_3
0.55	4.1	0.72	8.43	0.79	2.38	2.45	1.91	0.0036	0.00158	0.0141

The parameter values are shown in Table 5, and the calculation results are as follows:

$$E^* = (0.3131, 1.4843), \chi = -0.4312, \eta = 0.2461, \tau_0 = 0.3270, g_1 = 1.2869, g_2 = 1.7464.$$

The initial conditions are specified as follows:

$$u(x, y, 0) = u_* (1 + 0.1 (rand - 0.5)), v(x, y, 0) = v_* (1 + 0.1 (rand - 0.5)).$$

The outcomes of the numerical simulation indicate that speckle and mixed-structure patterns emerge in the graphical representation with this particular set of parameters, as illustrated in Figure 5.

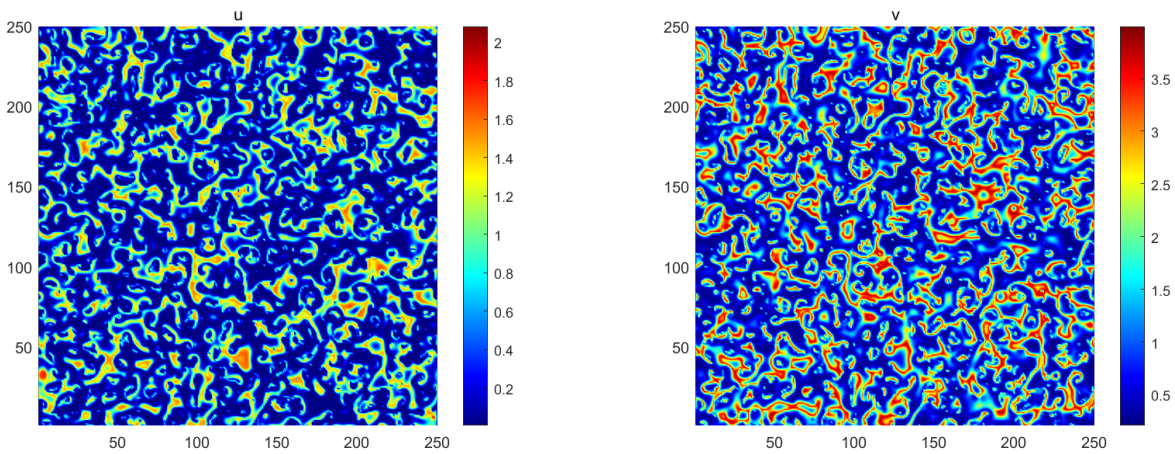

(a) Phytoplankton density distribution pattern.

(b) Zootoplankton density distribution pattern.

Figure 5. Density distribution pattern of system (2.1) at $\alpha = 0.55, \tau = 4.1, \zeta = 0.72, G = 8.43, n = 0.79, \kappa = 2.38, m = 2.45, d_1 = 0.0036, d_2 = 0.00158, d_3 = 0.0141$, and $\alpha_1 = \alpha_2 = 1$.

Now, we use the parameters in Table 5 and symmetric initial conditions to perform numerical simulations by changing parameters d_1, d_2, and d_3. Numerical simulation was carried out with other parameters remaining unchanged, and the results showed that there is a symmetric mixed structure solution. The subsequent figure illustrates the intricate pattern evolution of the symmetric mixed pattern across parameters. We select the following symmetric initial conditions:

$$u(x,y,0) = \begin{cases} u^*, & x,y \in (80,120), \\ u^* - 0.001, & other, \end{cases}$$

$$v(x,y,0) = \begin{cases} v^*, & x,y \in (80,120), \\ v^* - 0.001, & other. \end{cases}$$

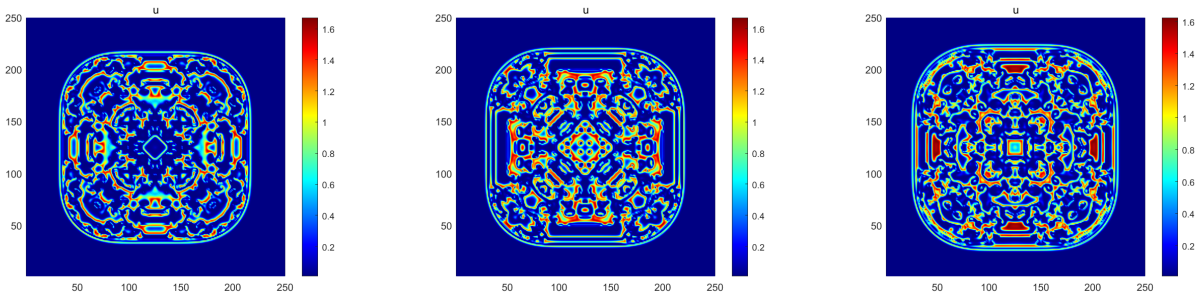

(a_1) $t = 10000$ and $d_2 = 0.003$ (a_2) $t = 10000$ and $d_2 = 0.004$ (a_3) $t = 10000$ and $d_2 = 0.005$

Phytoplankton density distribution pattern.

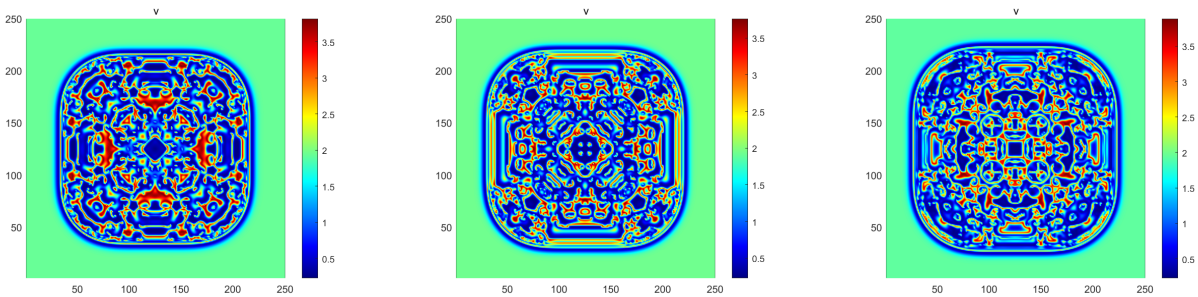

(b_1) $t = 10000$ and $d_2 = 0.003$ (b_2) $t = 10000$ and $d_2 = 0.004$ (b_3) $t = 10000$ and $d_2 = 0.005$

Zootoplankton density distribution pattern.

Figure 6. Population density distribution pattern of phytoplankton and zootoplankton with with different parameters $d_1 = 0.002$ and $d_3 = 0.018$.

Figure 6 shows the spatial distribution patterns of phytoplankton and zooplankton at different diffusion coefficients, d_2. The diffusion coefficient d reflects the influence of phytoplankton on the distribution of zooplankton. When $d_2 = 0.003$, phytoplankton and zooplankton form highly clustered patterns, with zooplankton closely following the prey. When $d_2 = 0.005$, phytoplankton and zooplankton are more dispersed, and the zooplankton pattern is more complex. This indicates that the diffusion ability of phytoplankton affects the hunting efficiency of zooplankton, and zooplankton tend

to migrate to areas with a high density of phytoplankton. When $d_2 = 0.004$, the distribution densities of phytoplankton and zooplankton are between the distribution densities of phytoplankton and zooplankton at $d_2 = 0.003$ and $d_2 = 0.005$.

Let $d_1 = 0.002, d_2 = 0.004$, and $d_3 = 0.015$ through the observation of the distribution pattern of plankton population density in Figure 7. At $t = 6000$, the system presents an incomplete pattern structure. Phytoplankton begins to form an irregular pattern distribution, while zooplankton shows an aggregation pattern following predation. At $t = 8000$, the pattern structure gradually forms a stable state. At $t = 10000$, the system reaches a stable state and forms a predator aggregation area that is misaligned with the plant pattern. We find that as time goes by, t, the distribution pattern of plankton population density becomes more complex. This indicates that the system presents a complex competitive process over time. This reflects the process by which the ecosystem reaches a stable state through dynamic adjustment.

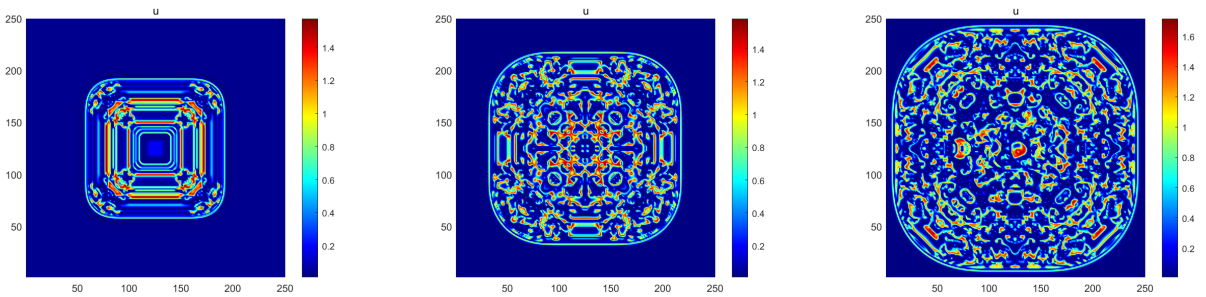

(a_1) $t = 6000$ (a_2) $t = 8000$ (a_3) $t = 10000$

Phytoplankton density distribution pattern.

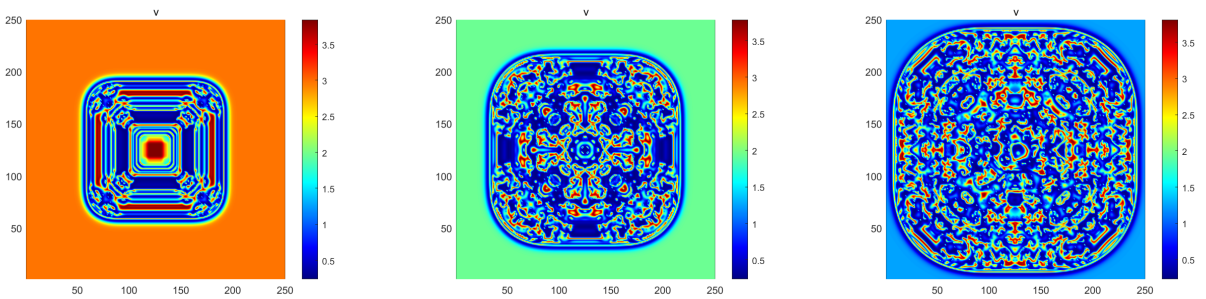

(b_1) $t = 6000$ (b_2) $t = 8000$ (b_3) $t = 10000$

Zootoplankton density distribution pattern.

Figure 7. The distribution patterns of phytoplankton and zooplankton population densities at different time periods.

Let parameter $d_1 = 0.002, d_2 = 0.004$, and $d_3 = 0.017$, the patterns of phytoplankton and zooplankton at different times are shown in Figure $8a_1 - a_4$ and Figure $8c_1 - c_4$. For diffusion coefficients at $d_1 = 0.002, d_2 = 0.006$, and $d_3 = 0.017$, the patterns of phytoplankton and zooplankton at different times are shown in Figure $8b_1 - b_4$ and Figure $8d_1 - d_4$. In Figure 8, the density of phytoplankton gradually increases over time. It can be seen from the pattern that the difference between the high-density area and the low-density area significantly increases. The internal structure

of the pattern becomes more complex, showing more details and layers. The distribution pattern of zooplankton shows a significantly misaligned predation aggregation area with that of plants, and the density of predation hotspots continues to increase over time. It can be seen from the pattern that the spatial distribution of phytoplankton and zooplankton shows complex dynamic behaviors.

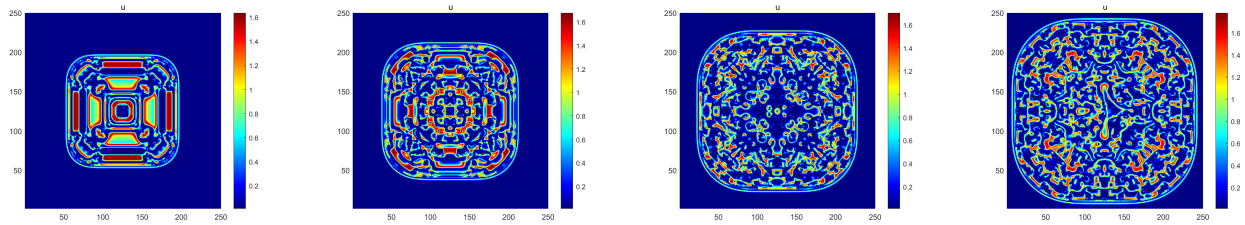

(a_1) $t = 6000$ and $d_2 = 0.004$ (a_2) $t = 9000$ and $d_2 = 0.004$ (a_3) $t = 12000$ and $d_2 = 0.004$ (a_4) $t = 15000$ and $d_2 = 0.004$

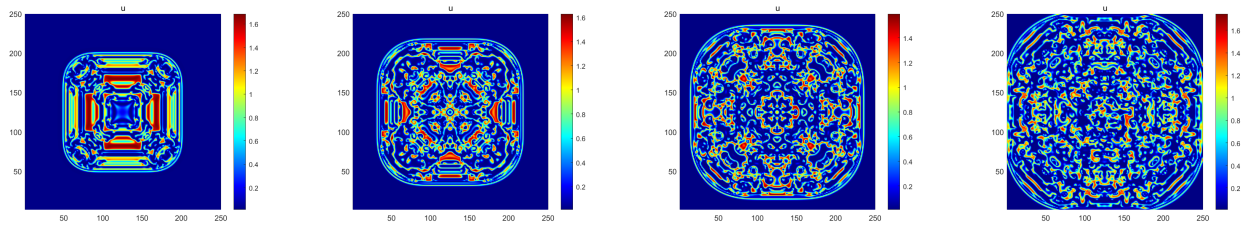

(b_1) $t = 6000$ and $d_2 = 0.006$ (b_2) $t = 9000$ and $d_2 = 0.006$ (b_3) $t = 12000$ and $d_2 = 0.006$ (b_4) $t = 15000$ and $d_2 = 0.006$

Population density distribution pattern of phytoplankton.

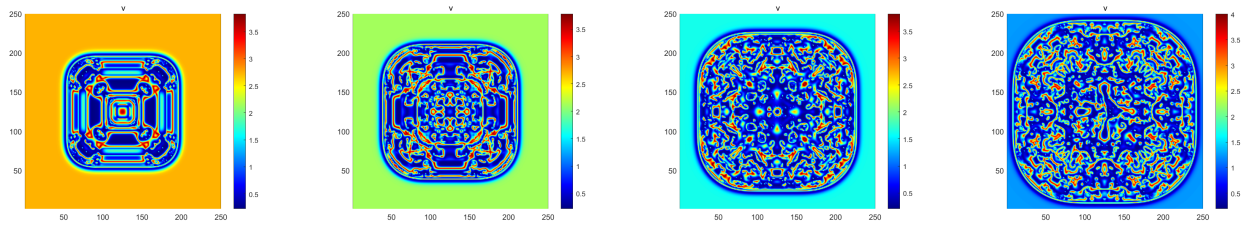

(c_1) $t = 6000$ and $d_2 = 0.004$ (c_2) $t = 9000$ and $d_2 = 0.004$ (c_3) $t = 12000$ and $d_2 = 0.004$ (c_4) $t = 15000$ and $d_2 = 0.004$

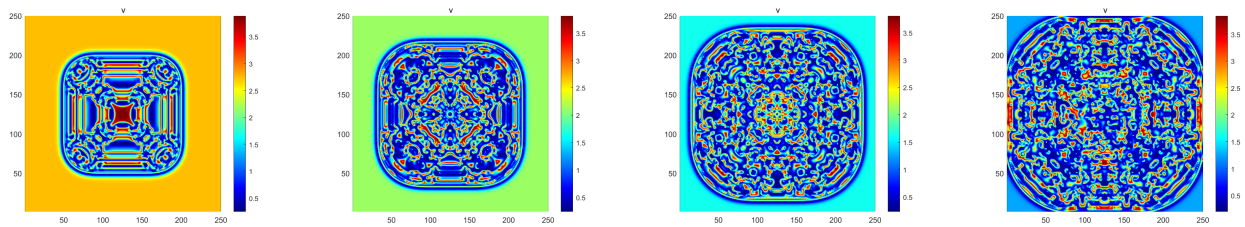

(d_1) $t = 6000$ and $d_2 = 0.006$ (d_2) $t = 9000$ and $d_2 = 0.006$ (d_3) $t = 12000$ and $d_2 = 0.006$ (d_4) $t = 15000$ and $d_2 = 0.006$

Zootoplankton density distribution pattern.

Figure 8. Population density distribution patterns of phytoplankton and zootoplankton with parameters $d_1 = 0.002$ and $d_3 = 0.017$.

Through the analysis of the patterns of phytoplankton and zooplankton, we see that, as time goes by, the patterns of zooplankton evolve from simple patterns to complex ones, demonstrating the complexity of this ecosystem. The diffusion coefficient is highly sensitive to the generation of patterns. A smaller diffusion coefficient leads to more regular and symmetrical patterns, while a larger diffusion coefficient results in more complex and irregular patterns, significantly affecting the distribution pattern of plankton. The initial conditions and diffusion coefficient significantly impact the long-term ecological behavior of the model. Moreover, initial conditions affect the formation of the pattern, while the parameters affect the distribution structure of the ecosystem.

5. Conclusions

We combine theoretical analysis with numerical simulation to deeply explore the dynamic behavioral characteristics of the fractional-order PZEM. In theoretical analysis, we conduct stability, Turing instability, Hopf bifurcation, and nonlinear analysis for the PZEM. In numerical methods, we develop a high-precision numerical method for fractional-order PZEM without diffusion terms and verify the superiority of this method through comparison with other methods. Moreover, an effective discretization method is established for the model with diffusion terms. The numerical simulation results not only verify the correctness of the theoretical analysis, but also demonstrate complex dynamic behaviors at different diffusion coefficients. Moreover, the system presents significantly different spatial pattern evolution characteristics. The results reveal that the diffusion coefficient is crucial to the generation of patterns. A bigger diffusion coefficient will lead to more complex and irregular pattern structures, which directly affects the spatial distribution patterns of plankton populations. Furthermore, the initial conditions and the diffusion coefficient have a decisive influence on the long-term ecological behavior of the model: The initial conditions affect the formation process of the pattern, while the diffusion coefficient affects the dynamic evolution of the pattern structure. In future work, we will explore the response mechanism of the system at the coupling effect of multiple factors, as well as the effect of dynamic behavior for fractional-order.

Author contributions

Conceptualization, Methodology, Software, Data, Formal analysis and Funding acquisition, Writing-original draft and writing-review and editing: Shuai Zhang, Hao Lu Zhang, Yu Lan Wang and Zhi Yuan Li. All authors have read and agreed to the published version of the manuscript.

Use of AI tools declaration

The authors declare they have not used Artificial Intelligence (AI) tools in the creation of this article.

Acknowledgments

This paper is supported by Doctoral research start-up Fund of Inner Mongolia University of Technology (DC2300001252) and the Natural Science Foundation of Inner Mongolia (2024LHMS06025).

Conflict of interest

The authors declare that there are no conflicts of interest regarding the publication of this article.

References

1. J. C. Macdonald, H. Gulbudak, Forward hysteresis and Hopf bifurcation in an Npzd model with application to harmful algal blooms, *J. Math. Biol.*, **87** (2023), 45. https://doi.org/10.1007/s00285-023-01969-7
2. H. Liu, C. J. Dai, H. G. Yu, Q. Guo, J. B. Li, A. M. Hao, et al. Dynamics of a stochastic non-autonomous phytoplankton-zooplankton system involving toxin-producing phytoplankton and impulsive perturbations, *Math. Comput. Simul.*, **203** (2023), 368–386. https://doi.org/10.1016/j.matcom.2022.06.012
3. K. Dehingia, A. Das, E. Hincal, K. Hosseini, The effect of time delay on the dynamics of a plankton-nutrient system with refuge, *Braz. J. Phys.*, **55** (2025), 28. https://doi.org/10.1007/s13538-024-01670-0
4. M. Xu, Y. Liu, Z. Zhao, K. Fu, X. Lv, Advancing parameter estimation with characteristic finite difference method (CFDM) for a marine ecosystem model by assimilating satellite observations: Spatial distributions, *Front. Mar. Sci.*, **9** (2022), 997537. https://doi.org/10.3389/fmars.2022.997537
5. A. W. Omta, E. A. Heiny, H. Rajakaruna, D. Talmy, M. J. Follows, Trophic model closure influences ecosystem response to enrichment, *Ecol. Modell.*, **475** (2023), 110183. https://doi.org/10.1016/j.ecolmodel.2022.110183
6. M. N. Huda, Q. Q. A'yun, S. Wigantono, H. Sandariria, I. Raming, A. Asmaidi, Effects of harvesting and planktivorous fish on bioeconomic phytoplankton-zooplankton models with ratio-dependent response functions and time delays, *Chaos Soliton Fract.*, **173** (2023), 113736. https://doi.org/10.1016/j.chaos.2023.113736
7. K. Chakraborty, K. Das, Modeling and analysis of a two-zooplankton one-phytoplankton system in the presence of toxicity, *Appl. Math. Model.*, **39** (2015), 1241–1265. https://doi.org/10.1016/j.apm.2014.08.004
8. Y. Lv, J. Cao, J. Song, R. Yuan, Y. Pei, Global stability and Hopf-bifurcation in a zooplankton-phytoplankton model, *Nonlinear Dyn.*, **76** (2014), 345–366. https://doi.org/10.1007/s11071-013-1130-2
9. V. P. Dubey, J. Singh, A. M. Alshehri, S. Dubey, D. Kumar, Numerical investigation of fractional model of phytoplankton-toxic phytoplankton-zooplankton system with convergence analysis, *Int. J. Biomath.*, **15** (2022), 2250006. https://doi.org/10.1142/S1793524522500061
10. P. Panja, T. Kar, D. K. Jana, Impacts of global warming on phytoplankton-zooplankton dynamics: A modelling study, *Environ. Dev. Sustain.*, **26** (2024), 13495–13513. https://doi.org/10.1007/s10668-023-04430-3
11. I. M. Suthers, A. J. Richardson, D. Rissik, The importance of plankton, in *Plankton: A Guide to Their Ecology and Monitoring for Water Quality*, Australia: CSIRO Publishing, 2019, 1–13. https://doi.org/10.1080/00288330.2019.1625497

12. W. Wang, S. Liu, D. Tian, D. Wang, Pattern dynamics in a toxin-producing phytoplankton-zooplankton model with additional food, *Nonlinear Dyn.*, **94** (2018), 211–228. https://doi.org/10.1007/s11071-018-4354-3

13. J. Alzabut, R. Dhineshbabu, A. G. M. Selvam, J. F. Gomez-Aguilar, H. Khan, Existence, uniqueness and synchronization of a fractional tumor growth model in discrete time with numerical results, *Results Phys.*, **54** (2023), 107030. https://doi.org/10.1016/j.rinp.2023.107030

14. W. AI-Sadi, Z. Wei, S. Q. T. Abdullah, A. Alkhazzan, J. F. Gomez-Aguilar, Dynamical and numerical analysis of the hepatitis B virus treatment model through fractal-fractional derivative, *Math. Methods Appl. Sci.*, **48** (2024), 639–657. https://doi.org/10.1002/mma.10348

15. M. S. Shabbir, Q. Din, M. De la Sen, J. F. Gomez-Aguilar, Exploring dynamics of plant-herbivore interactions: Bifurcation analysis and chaos control with Holling type-II functional response, *J. Math. Biol.*, **88** (2024), 8. https://doi.org/10.1007/s00285-023-02020-5

16. H. Khan, J. lzabut, J. F. Gomez-Aguilar, A. Alkhazan, Essential criteria for existence of solution of a modified-ABC fractional order smoking model, *Ain Shams Eng. J.*, **15** (2024), 102646. https://doi.org/10.1016/j.asej.2024.102646

17. N. Raza, A. Raza, Y. Chahlaoui, J. F. Gomez-Aguilar, Numerical analysis of HPV and its association with cervical cancer using Atangana-Baleanu fractional derivative, *Model. Earth Syst. Environ.*, **11** (2025), 60. https://doi.org/10.1007/s40808-024-02243-5

18. P. Li, R. Gao, C. Xu, Y. Li, A. Akgul, D. Baleanu, Dynamics exploration for a fractional-order delayed zooplankton-phytoplankton system. *Chaos Soliton Fract.*, **166** (2023), 112975. https://doi.org/10.1016/j.chaos.2022.112975

19. M. Javidi, B. Ahmad, Dynamic analysis of time fractional order phytoplankton-toxic phytoplankton-zooplankton system, *Ecol. Model.*, **318** (2015), 8–18. https://doi.org/10.1016/j.ecolmodel.2015.06.016

20. P. Kumar, V. Suat Erturk, R. Banerjee, M. Yavuz, V. Govindaraj, Fractional modeling of plankton-oxygen dynamics under climate change by the application of a recent numerical algorithm, *Phys. Scr.*, **96** (2021), 124044. https://doi.org/10.1088/1402-4896/ac2da7

21. C. P. Li, Z. Q. Li, Z. Wang, Mathematical analysis and the local discontinuous Galerkin method for Caputo-Hadamard fractional partial differential equation, *J. Sci. Comput.*, **85** (2020), 41. https://doi.org/10.1007/s10915-020-01353-3

22. C. P. Li, Z. Q. Li, The blow-up and global existence of solution to Caputo-Hadamard fractional partial differential equation with fractional Laplacian, *J. Nonlinear Sci.*, **31** (2021), 80. https://doi.org/10.1007/s00332-021-09736-y

23. C. Han, Y. L. Wang, Z. Y. Li, Novel patterns in a class of fractional reaction-diffusion models with the Riesz fractional derivative, *Math. Comput. Simul.*, **202** (2022), 149–163. https://doi.org/10.1016/j.matcom.2022.05.037

24. C. Han, Y. L. Wang, Z. Y. Li, A high-precision numerical approach to solving space fractional Gray-Scott model, *Appl. Math. Lett.*, **125** (2022), 107759. https://doi.org/10.1016/j.aml.2021.107759

25. C. P. Li, Q. Yi, A. Chen, Finite difference methods with non-uniform meshes for nonlinear fractional differential equations, *J. Comput. Phys.*, **316** (2016), 614–631. https://doi.org/10.1016/j.jcp.2016.04.039
26. X. H. Wang, H. L. Zhang, Y. L. Wang, Z. Y. Li, Dynamic properties and numerical simulations of the fractional Hastings–Powell model with the Grünwald-Letnikov differential derivative, *Int. J. Bifurcation Chaos*, **35** (2025), In press.
27. M. Singh, S. Das, Rajeev, S. H. Ong, Novel operational matrix method for the numerical solution of nonlinear reaction-advection-diffusion equation of fractional order, *Comput. Appl. Math.*, **41** (2022), 306. https://doi.org/10.1007/s40314-022-02017-8
28. M. Kashif, M. Singh, T. Som, E. M. Craciun, Numerical study of variable order model arising in chemical processes using operational matrix and collocation method, *J. Comput. Sci.*, **80** (2024), 102339. https://doi.org/10.1016/j.jocs.2024.102339
29. P. Roul, Design and analysis of efficient computational techniques for solving a temporal-fractional partial differential equation with the weakly singular solution, *Math. Methods Appl. Sci.*, **47** (2024), 2226–2249. https://doi.org/10.1002/mma.9744
30. T. Kumari, P. Roul, An efficient computational technique for solving a time-fractional reaction-subdiffusion model in 2D space, *Comput. Math. Appl.*, **160** (2024), 191–208. https://doi.org/10.1016/j.camwa.2024.02.018
31. Anjuman, A. Y. T. Leung, S. Das, Two-dimensional time-fractional nonlinear drift reaction-diffusion equation arising in electrical field, *Fractal Fract.*, **8** (2024), 456. https://doi.org/10.3390/fractalfract8080456
32. R. Sharma, A numerical study for nonlinear time-space fractional reaction-diffusion model of fourth-order, *J. Comput. Nonlinear Dyn.*, **20** (2025), 021001. https://doi.org/10.1115/1.4067065
33. K. M. Owolabi, S. Jain, E. Pindza, E. Mare, Comprehensive numerical analysis of time-fractional reaction-diffusion models with applications to chemical and biological phenomena, *Mathematics*, **12** (2024), 3251. https://doi.org/10.3390/math12203251
34. M. Sohaib, K. M. Furati, A. Shah, Space fractional Allen-Cahn equation and its applications in phase separation: A numerical study, *Commun. Nonlinear Sci. Numer. Simul.*, **137** (2024), 108173. https://doi.org/10.1016/j.cnsns.2024.108173
35. I. Petráš, *Fractional-Order Nonlinear Systems: Modeling, Analysis and Simulation*, Heidelberg: Springer Science & Business Media, 2011. https://doi.org/10.1007/978-3-642-18101-6
36. X. L. Gao, H. L. Zhang, X. Y. Li, Research on pattern dynamics of a class of predator-prey model with interval biological coefficients for capture,, *AIMS Math.*, **9** (2024), 18506–18527. https://doi.org/10.3934/math.2024901
37. D. Y. Xue, L. Bai, Numerical algorithms for Caputo fractional-order differential equations, *Int. J. Control*, **90** (2016), 1201–1211. https://doi.org/10.1080/00207179.2016.1158419
38. D. Y. Xue, C. N. Zhao, Y. Q. Chen, A modified approximation method of fractional order system, in *2006 International Conference on Mechatronics and Automation*, IEEE, Luoyang, (2006), 1043–1048. https://doi.org/10.1109/ICMA.2006.257769

39. D. Y. Xue, *Fractional Calculus and Fractional-Order Control*, Beijing: Science Press, 2018.

40. W. H. Deng, J. H. Lü, Design of multidirectional multiscroll chaotic attractors based on fractional differential systems via switching control, *Chaos*, **16** (2006), 043120. https://doi.org/10.1063/1.2401061

AIMS Press

© 2025 the Author(s), licensee AIMS Press. This is an open access article distributed under the terms of the Creative Commons Attribution License (http://creativecommons.org/licenses/by/4.0)